Time Domain Projection for Real-Time Side-Looking GP-SAR

Johannes Schlichenmaier
FindMine gGmbH
Illertissen, Germany
schlichenmaier@ieee.org

Bernd Arendt
FindMine gGmbH
Illertissen, Germany
bernd.arendt@findmine.org

Winfried Mayer
FindMine gGmbH
Illertissen, Germany
winfried.mayer@findmine.org

***Abstract*—The need for efficient mine and UXO clearance comes with the need for high-throughput examination of hazardous areas. This work proposes a time domain projection method, that combines the time-efficient measurements of side-looking SAR with an FFT-based approach for depth resolution. This allows for near real-time processing for the use in time-sensitive hazard protection, e.g. in the machine-assisted mine clearance. Measurements of actual hazardous objects in realistic scenarios and benchmarks show, that the increase in efficiency does not come with a compromise in detection capabilities compared to the standard backprojection method.**

***Index Terms*—GPR, GP-SAR, UAV, mine detection, mine clearance, signal processing**

I. Introduction

Despite ongoing global efforts of non-governmental and governmental demining organizations over the last decades, the amount of land contaminated by anti-vehicle mines (AVMs), anti-personnel mines (APMs), improvised explosive devices (IEDs), and unexploded ordnance (UXO) currently is growing bigger and bigger. This is due to the time and resource-costly act of clearing existing contaminated areas, and the continued deployment of these devices in ongoing conflicts [1], [2].

It is the opinion of the authors of this work, that—to answer the ever-growing clearing challenges of mines, IEDs, and UXO—future efforts will be greatly expedited with the help of radio-controlled or autonomous machinery. This trend is visible in affected areas, where more and more demining actors are working with machinery to increase the area throughput but also to ensure safety for their personnel, due to the emergence of increasingly devious disarming countermeasures seen in the field [3].

Although machinery can and do certainly help with the clearance effort [4], their usage is not cheap and even they can be damaged by hazards like anti-tank mines [5]. To increase the effectiveness of such machinery and to prevent downtime due to damage or destruction, a method to efficiently measure and process a large area before the clearing action, as well during, is needed.

For the last years, ground-penetrating radar (GPR) has been proven to be a promising technology to detect mines and other hazardous objects [6], [7]. Radar sensors provide a safe way to remotely detect irregularities on and below the ground. Contrary to metal detectors or magnetometers, their operation is also usually not disturbed by the presence of metallic objects outside of their respective field of view (FoV), which makes them easier to employ with machinery.

All authors contributed equally. We thank the Urs Endress Foundation for funding this work. Corresponding author: Johannes Schlichenmaier.

II. Problem Formulation and State of the Art

Generally, a GPR sensor is surveying an area and processing a volume under said area which can be represented by a grid of three-dimensional points $\vec{R}_{i,k,l}$ above and below the surface. The grid starts at the point $(x_0\ y_0\ z_0)^{\mathrm{T}}$ and extends for I, K, and L steps in all three dimensions with a spacing of Δx, Δy, and Δz respectively:

$$\vec{R}_{i,k,l} = \begin{pmatrix} x_i \\ y_k \\ z_l \end{pmatrix} = \begin{pmatrix} x_0 + i \cdot \Delta x \\ y_0 + k \cdot \Delta y \\ z_0 + l \cdot \Delta z \end{pmatrix}, \quad i \in I,\ k \in K,\ l \in L\ . \tag{1}$$

The sensor itself is usually placed above the surveyed area, e.g., by being mounted on an unmanned aerial vehicle (UAV), taking radar measurements at M positions along its trajectory. In this work, the measurement points $\vec{P}_{\mathrm{tr}}$ will be represented by the mid point between the position of the transmit antenna $(x_{\mathrm{t}}\ y_{\mathrm{t}}\ z_{\mathrm{t}})^{\mathrm{T}}$ and receive antenna $(x_{\mathrm{r}}\ y_{\mathrm{r}}\ z_{\mathrm{r}})^{\mathrm{T}}$:

$$\vec{P}_{\mathrm{tr},m} = \begin{pmatrix} x_{\mathrm{tr},m} \\ y_{\mathrm{tr},m} \\ z_{\mathrm{tr},m} \end{pmatrix} = \frac{1}{2} \cdot \begin{pmatrix} x_{\mathrm{t},m} + x_{\mathrm{r},m} \\ y_{\mathrm{t},m} + y_{\mathrm{r},m} \\ z_{\mathrm{t},m} + z_{\mathrm{r},m} \end{pmatrix}, \quad m \in M \tag{2}$$

For most applications, a radar measurement consists of a sampled version of the received and downconverted time signal, i.e., the intermediate frequency time signal s_{IF}. It corresponds to the frequency response of the channel, comprising the flight time of the signal from and to the objects in the surveyed area and the response from the objects themselves.

Fig. 1 gives a schematic overview of the measurement concept for a side-looking ground-penetrating synthetic aperture radar (GP-SAR). The challenge lies in resolving the received signal power for each point $\vec{R}_{i,k,l}$ of the grid using the available measurements from the measurement points $\vec{P}_{\mathrm{tr},m}$. This has to be done with a large enough area throughput for the measurement itself as well as the processing, with

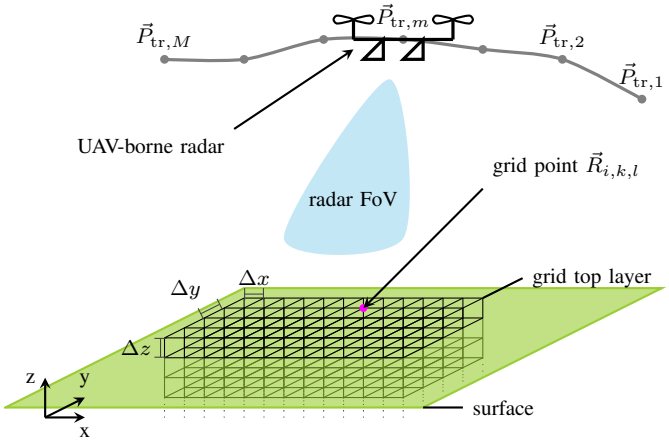

Fig. 1. A UAV-borne side-looking GP-SAR sensor is taking measurements at positions $\vec{P}_{\mathrm{tx},m}$ of an area inside its field of view (FoV). The SAR-processed volume is represented by grid points with spacings of Δx, Δy, and Δz.

enough spatial resolution to distinguish buried objects from their surroundings and allow for detection later on.

The main restricting factor for the application in real-life scenarios is time. Measurements have to cover a large enough area in an appropriate time frame, while minimizing potential damage to the sensor—or even worse—danger to personnel. Additionally, processing has to be fast enough to allow for the system to being used on location, while providing a fine enough resolution to enable detection of objects.

Several promising approaches—mainly with UAV-mounted radar sensors—have been presented in the last couple of years. In [7], [8], it has been shown, that circular SAR processing based on backprojection is able to sufficiently resolve the grid to allow for detection of various buried objects, like APMs and AVMs, filled canisters, and even tripwires used for triggering explosive devices. By using SAR, the side-looking radar sensor only needs a single channel to resolve the signal spatially and the UAV can be flown several meters above ground. This increases ground coverage per flight time and makes the flight control very simple and the operation relatively safe.

However, the backprojection algorithm incurs a large computational cost, due to the huge amount of correctional terms to calculate—one for each grid point/measurement position combination taken into account. In [9], an approach based on compressed sensing is used to decrease the number of measurement points while retaining clutter levels.

In [6], a down-looking multi-channel GPR is used to detect buried objects. In [10], a similar approach is presented, using Delaunay interpolation and phase shift migration (PSM) of the measurements to enable fast Fourier transform (FFT) processing, reaching real-time potential. However, in both these cases, the radar sensor has to fly low over the ground in very narrow strips, severely decreasing ground coverage per flight time and increasing the difficulty of flight planning and control.

III. Time Domain Projection SAR Method

The algorithm proposed in this work seeks to combine the advantages of FFT on the processing time with those of a higher flying SAR algorithm, e.g., the much greater ground coverage per flight time, the larger freedom in trajectory planning and the higher tolerance against flight path inaccuracies.

This is achieved by transforming the measured time signals from the actual arbitrary measurement points to the top layer of the equidistant grid $\vec{R}_{i,k,0}$ from Fig. 1, in a process similar to an antenna far-field to near-field transformation using elements of the backprojection approach. Subsequently, the now transformed signals approximate those of a down-looking radar sensor taking measurements very low to the ground at the top layer grid positions, allowing for the use of FFT to resolve the z-dimension quickly.

A. Signal Model

For a linearly ramped frequency modulated continuous wave (FMCW) radar, the frequency of the transmitted signal f_{t} is described by

$$f_{\mathrm{t}}(t) = f_0 + \frac{B}{T_{\mathrm{r}}} t \tag{3}$$

with the starting frequency of f_0, the used bandwidth B, and the ramp duration T_{r}.

The time of flight τ of the signal from the radar sensor at a tx/rx-position described by (2) to a presumed target at one of the top layer points from (1) is given by

$$\tau = \frac{2 \cdot \left\| \vec{P}_{\mathrm{tr},m} - \vec{R}_{i,k,0} \right\|}{c} \ . \tag{4}$$

As per [11], the intermediate time signal for a FMCW radar $s_{\mathrm{IF}}(t)$ can be described by

$$s_{\mathrm{IF}}(t) = \cos(\Delta\varphi(t)) \ , \tag{5}$$

with the phase of the signal for a single target of

$$\Delta\varphi(t) = 2\pi \cdot \left(f_0\tau + \frac{B}{T_{\mathrm{r}}} t\tau + \frac{B}{2T_{\mathrm{r}}} \tau^2 \right) \ . \tag{6}$$

As all the subsequent corrections and calculations are done in the digital domain after sampling N_{s} samples with the sampling frequency f_{s}, it is useful, to convert the relevant equations from the continuous time domain into a sampled time domain with time steps

$$t_n = \frac{n}{f_{\mathrm{s}}} = n \cdot \Delta t_{\mathrm{s}}, \quad n \in N_{\mathrm{s}} \ . \tag{7}$$

Subsequently, the frequency of the transmitted signal at each time step t_n is given by

$$f(t_n) = f_n = f_0 + \frac{B}{T_{\mathrm{r}}} t_n \Leftrightarrow t_n = \frac{T_{\mathrm{r}}}{B} f_n - f_0 \ . \tag{8}$$

Substituting $t \rightarrow t_n$ in (6) and further plugging in (8) yields the transmit frequency dependant phase change of the intermediate time signal due to the time of flight as

$$\Delta\varphi(f_n) = 2\pi \cdot \left(f_n \tau + \frac{B}{2T_\mathrm{r}} \tau^2 \right) \quad . \tag{9}$$

B. Top layer projection and depth compression

To transform the recorded measurement signals into the top layer time signals $s_{\mathrm{TL},i,k}(f_n)$, all recorded signals $s_{\mathrm{IF},m}(f_n)$ for each top layer grid point $\vec{R}_{i,k,0}$ are first phase corrected with (9) and then summed up as per

$$s_{\mathrm{TL},i,k}(f_n) = \sum_{m=1}^{M} \frac{1}{\alpha_{m,i,k}} \cdot s_{\mathrm{IF},m}(f_n) \cdot e^{-j \cdot \Delta\varphi(f_n)} \quad . \tag{10}$$

The term α in (10) represents a combination of general compensation terms for channel influences like free-space attenuation, or the influence of the FoV of the sensor antennas.

The depth compression can be simply done with an FFT of the top layer time signals, resolving the depths from the top layer down with a actual step size of

$$\Delta z_{\mathrm{act}} = \frac{c \cdot f_\mathrm{s} \cdot T_\mathrm{r}}{2 \cdot (\frac{N_\mathrm{FFT}}{2} - 1) \cdot B} \overset{!}{\lesssim} \Delta z \tag{11}$$

The actual step size can therefore be adjusted as necessary to using zero-padding in the FFT to either be smaller than a set value, or to be always within a certain range (e.g., 10 %) of a depth step. The maximum depth can be restricted to the range of interest by downsampling the time signals beforehand.

The top layer of the grid is usually chosen some decimeters above the actual surface, with the grid reaching down several decimeters below ground. Technically it is possible to consider the influence of the ground on the signal. However, this mainly leads to a perceived depth shift of a few centimeters, which for potentially hazardous objects in the ground is of less concern, than actually detecting them, and is therefore omitted in this work.

IV. Measurements

To verify the suggested method, measurements were done with an UAV-based side-looking radar sensor—further developed from the one used in [7]—and processed using the time domain projection (TP) and the backprojection (BP) SAR algorithms.

The sensor was equipped with two horizontally and two vertically polarized antennas, although only the horizontal co-polarization was used for evaluation. A frequency range of 0.9 GHz to 2.4 GHz was chosen for a good trade-off between spatial resolution and ground-penetration capability.

The actual position of the UAV along the trajectory was determined by fusing intertial measurement unit (IMU) and real-time kinematic (RTK) positioning data, providing sub-centimeter accuracy. A pre-calculated, geolocalized digital surface model (DSM) served as reference for the surface height at each point of the processed grid.

The flight trajectory (Fig. 2) was chosen as two squares (rotated by 45°) such that the swath width of the antenna beam covered the evaluation area of $5 \times 5\,\mathrm{m}^2$.

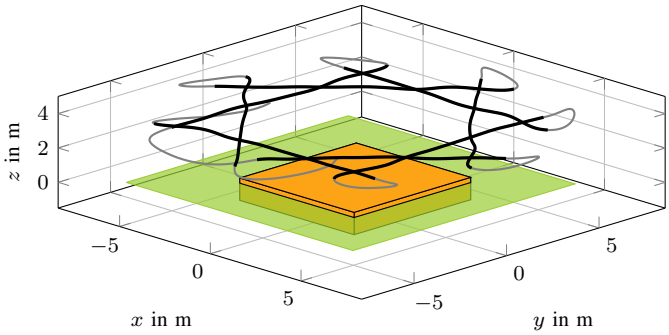

Fig. 2. Flight trajectory (full: ——, used: ——) and evaluated grid area (▭) above and below the surface (▭).

Fig. 3. Reference measurement consisting of four steel spheres above the ground at different heights.

The full measurement flight duration was 77 s, although, by design, the reference trajectory is very inefficient. The speed of the UAV and thus the area coverage per time can be increased significantly for larger trajectory legs.

For the evaluation, the top layer—i.e., the projection layer—was chosen at 0.35 m above ground. The grid spacings were set at $\Delta x = \Delta y = 0.05\,\mathrm{m}$ and $\Delta z = 0.01\,\mathrm{m}$, with a maximum depth of 0.4 m below ground.

A. Reference measurements

Fig. 3 shows the reference measurement setup of four steel spheres with diameters of 7 cm and 9 cm on top of sandy soil. Two of the targets were placed directly on the ground, the other two atop plastic stands at a height of 0.08 m above ground.

Per leg of the two trajectory squares, around 180 measurements along the legs were combined for the evaluation, totalling just over 1400 radar measurements. For the TP-SAR, the time signal for each of these measurements could be downconverted by a factor of 8 to around 450 samples because of the lower maximum range requirement originating from the top layer. This reduction is not possible for the BP-SAR.

The comparing intensity plot for TP- and GP-SAR at 0.25 m above ground can be seen in Fig. 4. The height offset is in part due to inaccuracies of the underlying surface model and the unevenness of the sand. The four spheres are clearly visible

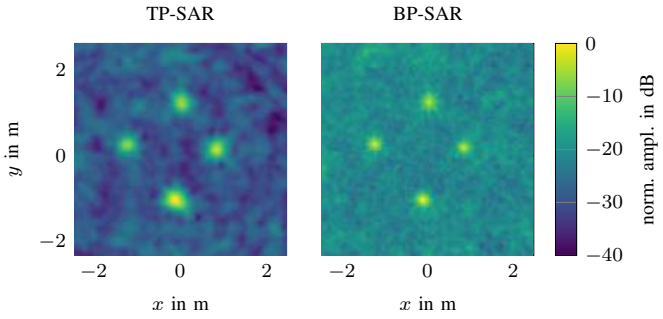

Fig. 4. Reference measurement intensity.

Fig. 5. The measurement system in flight over one of the CTRO Benkovac test areas [12].

in both cases, however, the mean signal to clutter ratio (SCR) for the TP-SAR is much higher at 20 dB to 30 dB, even if the spheres are positioned at slightly different heights. This is to be expected, as the spherical form and the very good reflective properties of the objects lead to a widening of their radar response.

Compared to the BP-SAR result, the TP-SAR exhibits a much more even SCR behaviour with clearer, albeit more spread out target intensities. This can be attributed to the measured signal fanning out over the depths due to the aspect angle of the sensor. This acts as a smoothing filter in x- and y-direction and—as will be shown with the other measurements—is not detrimental to target detection. In certain scenarios it even improves detection capability.

B. Actual clearance objects

To test the detection capabilities of the system and the processing method, several measurements were conducted at the Benkovac test site of the Croation Mine Action Centre (CTRO) [12]. Fig. 5 shows the system in flight over the test site. The test site comprises several test squares with predominantly dry soil, covered by dry grass.

The first measurement is of a full-metal TMM-1 AVM (Fig. 6(a)), with a diameter of 30 cm and a height of 9 cm. For TP-SAR, the intensity plot in Fig. 7 shows a clearly visible hot spot at the expected target position at around 0.18 m

(a) Metal AVM TMM-1 [13]. (b) Minimum-metal AVM TMA-4 [14]. (c) Minimum-metal APM PMA-3 [15].

Fig. 6. Mines used in the measurements at the CTRO Benkovac test site [12].

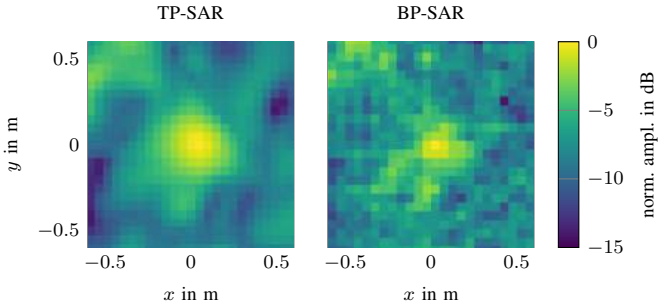

Fig. 7. Intensity plot of TMM-1 measurement at 0.18 m below ground.

below ground with an SCR of $\sim 6\,\mathrm{dB}$. The same hot spot is visible for the BP-SAR method. However it is smaller and more speckled, leading to a slightly decreased SCR of $\sim 4\,\mathrm{dB}$ to $6\,\mathrm{dB}$.

The next measurement is of a minimum-metal TMA-4 AVM (Fig. 6(b)) with a diameter of 28.4 cm and a height of 11 cm. The only metal parts in this mine are the three detonators hidden below the three plastic caps. Despite this, with the TP-SAR method, the target is clearly distinguishable from the surroundings at around 0.17 m below ground (Fig. 8) with an SCR of $\sim 6\,\mathrm{dB}$ to $10\,\mathrm{dB}$.

As for the previous measurement, the target is visible with the BP-SAR, however, the image is more speckled and with a decreased SCR. It should be noted, that the smoothing effect of the TP-SAR method does not remove clearly separated details like the hot spots left and above the main hot spot.

The final measurement presented is of a minimum-metal PMA-3 APM (Fig. 6(c)) with a diameter of 11.1 cm and a

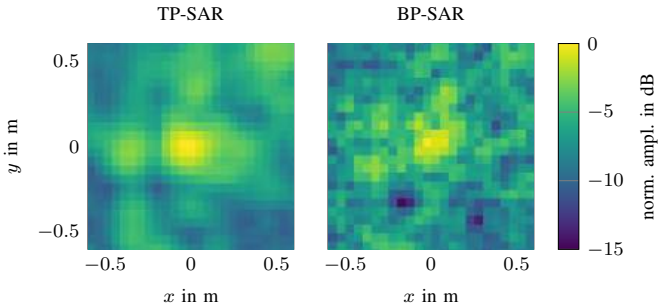

Fig. 8. Intensity plot of TMA-4 measurement at 0.17 m below ground.

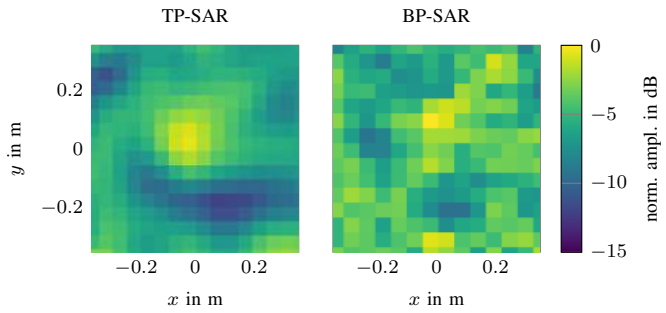

Fig. 9. Intensity plot of PMA-3 measurement at 0.03 m below ground.

TABLE I
BENCHMARK TIME RESULTS FOR TP- AND BP-SAR METHOD.

Method	step size in m	N_{depths}	N_{FFT}	Processing time in s
TP-SAR	0.01	100	16384	2.29
	0.005	200	32768	2.61
BP-SAR	0.01	100	16384	9.68
	0.005	200	16384	19.36

height of 4 cm. The mine is made from plastic and explosive and only has a small metal content as part of the detonator. Although the hot spot in the intensity plot at a depth of around 0.03 m below ground shown in Fig. 9 is not as pronounced as in the other two examples ($\sim$ 3 dB to 4 dB), it shows, that even a minimum-metal APM covered by a patch of grass can be detected by the TP-SAR method. By comparison for the BP-SAR method the target is hardly distinguishable from the background speckle.

C. Processing time benchmarks

To measure the processing cost of the parallelized time domain projection SAR (TP-SAR) method compared to an optimized and parallelized backprojection (BP-SAR) method, an area of 2x4 m was evaluated with a grid spacing of $\Delta x, y = 0.05\,\text{m}$. To simulate realistic settings, the top grid layer height was set to 0.1 m above ground, to make up for inconsistencies of the ground level and to catch potential hazardous objects laying on the ground. The grid extended down to 0.9 m below ground, to compensate for an increase in ground's relative permittivity which can be as assumed as high as $\varepsilon_\text{r} = 10$, which leads to a depth-compression by a factor of $\sqrt{\varepsilon_\text{r}} \approxeq 3.16$.

The number of depths N_{depths} was chosen at 100 and—to compensate for the depth compression—at 200. For the TP-SAR, the number of FFT-sampling points N_{FFT} was chosen, so that the requested depths could be achieved with a maximum deviation of $\sim 10\,\%$ of the step size. For simply achieving a step size smaller than the requested one, much fewer FFT-sampling points would be needed. The number of FFT-sampling points for the BP-SAR method was chosen high enough for the backprojection to reliably create useable intensity data for the objects.

The timing results for the pure processing of the full area based on 1411 measurements points $P_{\text{tr},m}$ are shown in Table I. The TP-SAR method shows a clear improvement over the BP-SAR method. This is especially true for an increased number of evaluated depths, which come with a negligible increase in processing time. As the wavelength of radar signals gets shorter with a higher relative permittivity below the surface, this allows for an increased depth resolution even in damper soil without incurring a high computational cost.

V. CONCLUSION

In this work, the TP-SAR algorithm is presented. It uses a projection of measurement signals recorded from an arbitrary flight trajectory in the time domain down to an equidistant grid close to the surface, similar to a near-field to far-field transformation known from antenna theory. This allows for a very fast and very fine depth resolution using an FFT, compared to the traditional back-projection, useful in soil with a higher dielectric constant, e.g., due to a higher water content.

Measurements of real mines show the improvement in image clarity and effectiveness of the method to detect such objects, while decreasing computing time.

Combined with the advantage, that measurements can be performed from several meters above the ground, making both flight planning and controlling much simpler, as well as expediting measurement time and ground coverage, the approach of TP-SAR shows great potential towards real-time measurements and processing for time-critical scenarios, such as automated mine clearance and hazard avoidance.

REFERENCES

[1] I. Osmolovska, "Walking on Fire: Demining in Ukraine," GLOBSEC Kyiv Office, Tech. Rep., Apr. 2023. [Online]. Available: https://www.globsec.org/what-we-do/publications/walking-fire-demining-ukraine
[2] "FSD Annual Report 2023," Tech. Rep., 2023.
[3] I. Osmolovska and N. Bilyk, "Cleaning the Augean Stables Demining Ukraine," GLOBSEC Kyiv Office, Tech. Rep., Jan. 2024. [Online]. Available: https://www.globsec.org/what-we-do/publications/cleaning-augean-stables-humanitarian-demining-ukraine
[4] Fondation suisse de déminage, "FSD Activity Report 2024," Tech. Rep., Mar. 2025. [Online]. Available: https://fsd.ch/wp-content/uploads/2025/03/FSD-ACTIVITY-REPORT-2024-EN.pdf
[5] "Tiller repaired in one week and back in the field thanks to our in-country workshop," https://gcs.ch/news-and-stories/2024/11/28/tiller-repair-in-under-a-week-thanks-to-our-in-country-workshop, Nov. 2024.
[6] M. Garcia-Fernandez, Y. A. Lopez, and F. L.-H. Andres, "Airborne Multi-Channel Ground Penetrating Radar for Improvised Explosive Devices and Landmine Detection," *IEEE Access*, vol. 8, pp. 165 927–165 943, 2020.
[7] A. Grathwohl, M. Stelzig, J. Kanz, P. Fenske, A. Benedikter, C. Knill, I. Ullmann, I. Hajnsek, A. Moreira, G. Krieger, M. Vossiek, and C. Waldschmidt, "Taking a Look Beneath the Surface: Multicopter UAV-Based Ground-Penetrating Imaging Radars," *IEEE Microwave Magazine*, vol. 23, no. 10, pp. 32–46, Oct. 2022.
[8] M. Schartel, R. Burr, R. Bahnemann, W. Mayer, and C. Waldschmidt, "An Experimental Study on Airborne Landmine Detection Using a Circular Synthetic Aperture Radar," p. 7.
[9] C. Bonfert, E. Ruopp, and C. Waldschmidt, "Improving SAR Imaging by Superpixel-Based Compressed Sensing and Backprojection Processing," vol. 62, pp. 1–12. [Online]. Available: https://ieeexplore.ieee.org/document/10491303/?arnumber=10491303
[10] M. Garcia-Fernandez, G. Alvarez-Narciandi, J. Laviada, Y. A. Lopez, and F. Las-Heras, "Towards real-time processing for uav-mounted gpr-sar imaging systems," *ISPRS Journal of Photogrammetry and Remote Sensing*, vol. 212, pp. 1–12, Jun. 2024.

[11] V. Winkler, "Range Doppler detection for automotive FMCW radars," in *2007 European Radar Conference*, Oct. 2007, pp. 166–169.
[12] "Benkovac Test Site," https://www.ctro.hr/test-site/benkovac-test-site.
[13] "CAT-UXO - TMM-1 landmine," https://cat-uxo.com/explosive-hazards/landmines/tmm-1-landmine.
[14] "CAT-UXO - TMA-4 landmine," https://cat-uxo.com/explosive-hazards/landmines/tma-4-landmine.
[15] "CAT-UXO - PMA-3 landmine," https://cat-uxo.com/explosive-hazards/landmines/pma-3-landmine.